J. Fluid Mech. (2012), *vol.* 707, *pp.* 307–330.
doi:10.1017/jfm.2012.280

Contact line dynamics and boundary layer flow during reflection of a solitary wave

Yong Sung Park[1]†, Philip L.-F. Liu[2,3] and I-Chi Chan[2]

[1] Division of Civil Engineering, University of Dundee, Dundee DD1 4HN, UK

[2] School of Civil and Environmental Engineering, Cornell University, Ithaca, NY 14853, USA

[3] Institute of Hydrological and Oceanic Sciences, National Central University, Jhongli, Taoyuan 320, Taiwan

(Received 9 December 2010; revised 4 April 2012; accepted 7 June 2012; first published online 13 July 2012)

In this paper we present a set of wave flume experiments for a solitary wave reflecting off a vertical wall. A particle tracking velocimetry (PTV) technique is used to measure free-surface velocity and the velocity field in the vicinity of the moving contact line. We observe that the free surface undergoes the so-called rolling motion as the contact line moves up and down the vertical wall, and fluid particles on the free surface almost always flow toward the wall except at the end of the reflection process. As the contact line descends along the wall, wall boundary layer flows move in a downward direction and therefore the boundary layer acts like a conduit through which the surface-rolling-induced flow escapes from the meniscus. However, during the last phase of the reflection process flow reversal occurs inside the wall boundary layer. An approximate analytical solution is developed to explain the flow reversal feature. Very good agreement between the approximate theory and measured data is obtained. Because of the flow reversal, boundary layer flows collide with the surface-rolling-induced flows. The collision gives rise to a jet ejecting from the meniscus into the water body, which later evolves into a small eddy. It is noticed that the fluid particles in different regions such as the free stream, the free-surface boundary layer and the wall boundary layer, can be transported to other regions by passing through the meniscus.

Key words: boundary layer structure, contact lines, solitary waves

1. Introduction

In a laboratory experiment for a surface solitary wave reflecting off a vertical wall in a two-dimensional wave flume, for a wave height-to-water depth ratio ($\epsilon = H'/h'$) ranging from 0.11 to 0.45 in $h' = 10$ cm, we observe that an eddy is formed near the meniscus and left behind the reflected wave. In figure 1, we show the trajectory of a seeding particle that is initially observed within the moving meniscus during the descending phase of the reflection for the case with $\epsilon = 0.45$. Note that the coordinate system in figure 1(*b*) is such that the undisturbed water body without the capillary effect would occupy the region where $x' \leqslant 0$ and $z' \leqslant 0$ (see also figure 4). At the first instant of tracking, which is labelled (i) in figure 1(*b*), the particle is found within

† Email address for correspondence: y.s.park@dundee.ac.uk

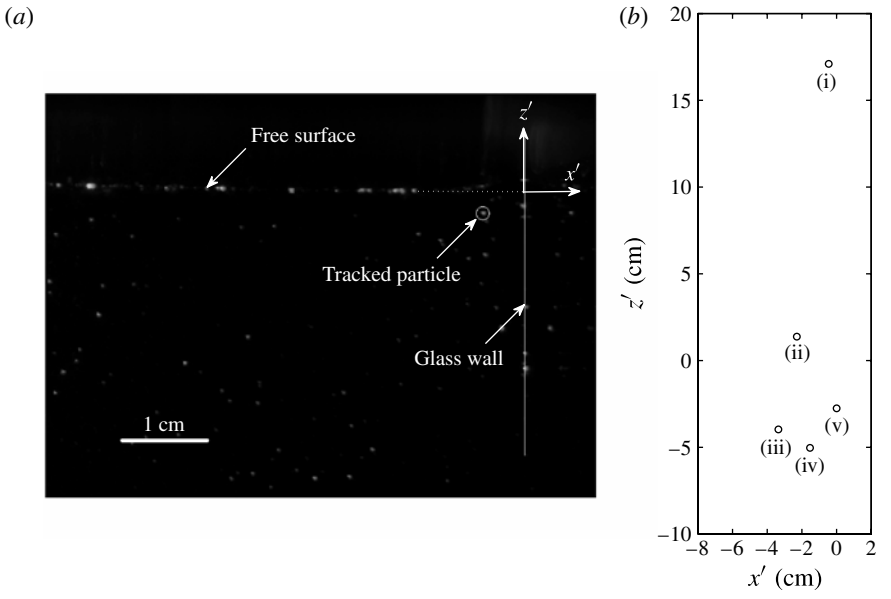

FIGURE 1. Tracking of a seeding particle marked by a circle in (*a*) during the reflection of a solitary wave with $\epsilon = 0.45$ in $h' = 10$ cm. The circles in (*b*) denote instantaneous locations of the particle during the final phase of the reflection process, which are numbered in the order of time at every tenth of a second. At first, the particle is observed within the meniscus which is moving downward (i). Near the end of reflection, the particle is ejected from the meniscus (ii)–(iii) and later entrained in upward moving boundary layer flows (iv)–(v). Note that (*a*) is taken at the moment corresponding to (iii) in (*b*).

the downward-moving meniscus. A tenth of a second later, when the solitary wave is almost completely reflected, the particle is ejected out of the meniscus down into the water body (ii). It travels further downwards and away from the wall (iii) before it is entrained in the upward-moving wall boundary layer flow ((iv) and (v)). To explain the origin of the eddy is the primary objective of this paper.

The range of H'/h' in our experiments falls into the simple reflection regime according to McHugh & Watt (1998), which is characterized by a lack of surface disturbance, droplet or even spray that is seen during the reflection of waves with higher amplitudes. Although the solitary waves under consideration are also sufficiently large that the surface tension effects can be neglected in most situations, those effects will be important near the meniscus where the eddy is observed. At this point, it is useful to consider two relevant length scales. The problem involves the boundary layer along the vertical wall with the length scale $l'_\nu \equiv (\nu' T')^{1/2}$, where ν' is the kinematic viscosity and T' is the time scale of reflection (for details see § 3). Also included in the problem is the moving contact line, which is defined as the intersection of the free surface and the solid boundary. There, capillary length may be chosen as the length scale, that is, $l'_\sigma \equiv (\sigma'/\rho' g')^{1/2}$, where σ' is the surface tension, ρ' is the density of the fluid, and g' is the gravitational acceleration. With $T' = O(1\text{ s})$ and $\sigma' = O(0.1\text{ N m}^{-1})$, both length scales are of $O(1\text{ mm})$ and comparable to each other. Therefore one can expect that the interaction of the wall boundary layer flow with the contact line dynamics plays an important role in the generation of the observed eddy.

Reflection and collision of solitary waves have been studied extensively during the last few decades. Chan & Street (1970) studied reflections of solitary waves at a vertical wall by solving the Navier–Stokes equation with a free-surface tracking scheme. The numerical result was consistent with the experimental data in terms of run-up height, where the maximum run-up was larger than twice the initial wave height. Maxworthy (1976) also observed in his experiments that the maximum water surface elevation was larger than twice the wave height and there was a time delay during the interaction. Those results have become recurring themes in subsequent studies (see e.g. Craig *et al.* 2006). Another striking feature of the solitary wave reflection/collision was added by Su & Mirie (1980), who observed dispersive trailing waves behind the solitary waves after the collision from their third-order perturbation solution for the Boussinesq equation. Byatt-Smith (1988, 1989) made similar observations by solving two weakly coupled KdV equations. He also noticed slight changes in the heights of the solitary waves after interactions. The aforementioned results have been confirmed in more recent theoretical works (e.g. Cooker, Weidman & Bale 1997; Craig *et al.* 2006), in which the full Euler equation for the potential fluid flow is solved. Note that neither viscosity nor capillarity has been considered in this context.

A more relevant body of literature is found in the area of capillary–gravity waves. Hocking suggested a simple wetting model, in which the dynamic contact angle varies with the speed of the contact line relative to the boundary, and studied wave generation at a vertically oscillating solid boundary (Hocking 1987*b*) and reflection at a stationary boundary (Hocking 1987*c*). Later Miles (1990) expanded Hocking's theory by adding viscous effects to the analysis and allowing a phase difference between the contact angle and the velocity of the contact line relative to the wall. To resolve the singularity of unbound shear force at the moving contact line that arises if the no-slip condition is applied there (see e.g. Dussan & Davis 1974), Miles (1990) used a slip boundary condition in which the slip velocity is proportional to the shear stress in the region very close to the contact line. Miles (1990) illustrated that Hocking's model is compatible with the slip boundary condition only if the amplitude of the contact-line motion is negligibly small. For the waves considered in Miles's (1990) analysis, l'_ν is much smaller than l'_σ due to the high wave frequency, and the interaction of the meniscus with viscous boundary layers was not investigated. Ting & Perlin (1995) carried out a series of experiments on flows near the contact line at a vertically oscillating plate. Although the amplitudes of the plate displacement were kept low (0.5–6 mm) and the contact angle was always less than 90°, the experimental cases include both stick and stick–slip motion of the contact line relative to the moving plate. It is noted that they also observed a vortex that changes its rotational direction over the period of plate oscillation for the case with stick–slip contact line motion, while no such vortex was present for the other case. However, no further description or explanation of the flow in the vicinity of the meniscus was given.

Motivated by engineering applications such as thin-film coating on a solid surface, most studies on the moving contact line have focused on steady flows of very low velocities (for a review see Dussan 1979), which may be readily described by lubrication theory (Eggers & Stone 2004). Hocking & Davis (2002) studied inertial effects on a spreading drop when the radius of the drop approaches its terminal value exponentially in time or when the drop is supported by a plate under an oscillatory motion in its own plane. Those examples were chosen to retain the simplicity of lubrication theory, and the focus of the study was to relate the macroscopic dynamic contact angle to the speed of the contact line. Cox (1998) also investigated the effects

of inertia on the contact angle in a situation where a liquid viscous boundary layer is present even close to the contact line, while the inviscid region above the boundary layer is stationary with respect to the steadily moving contact line.

Due to the highly unsteady nature of the flow in the present discussion, however, no direct comparison with the previous theoretical works is possible. Instead a detailed and quantitative description of the flow in the vicinity of the moving contact line has been made to identify the origin of the eddy associated with the reflection of a solitary wave. It will be shown that the moving contact line accompanies the rolling motion of the free surface (Dussan & Davis 1974), and its interaction with the unsteady boundary layer flow gives rise to the eddy.

The experimental setup is described in the following section. Both free-surface motions and the wall boundary layer flow around the moving contact line were measured by quantitative flow visualization techniques. In § 3, the measured boundary layer flows are presented and compared with the theoretical prediction. Then the flow induced by the moving contact line and its interaction with wall boundary layer flows are discussed in § 4. Finally, concluding remarks are made in § 5.

2. Experiments

2.1. *Experimental setup*

The experiments were conducted in the wave flume (32 m long, 0.6 m wide and 0.9 m deep) in the DeFrees Hydraulics Laboratory at Cornell University. The flume has glass sidewalls and a painted steel bottom. One section of the flume (∼14.5 m from the initial position of the wave maker) is fitted with a 1 m long clear acrylic bottom allowing the delivery of laser light from below for quantitative flow visualization techniques. The flume is equipped with a newly constructed piston-type wave maker consisting of a hydraulic cylinder (Parker HMI series) with a 4 m long rod, which is controlled by a high-precision proportional DC valve (Parker D41FH). The sensitivity of the valve is 0.05 % or 2 mm, and the maximum speed of the piston exceeds 2 m s^{-1}. Three ultrasonic wave gauges (Banner Engineering S18U) were used to measure water surface profiles at a sampling rate of 100 Hz. A PIV/PTV (particle image velocimetry, particle tracking velocimetry) system was employed for the velocity measurements. The locations of measurements are shown in figure 2.

For the reflection experiments a glass wall was installed above the false bottom (see figure 2*b*). A separate set of experiments on the head-on collision of two solitary waves with equal heights was also carried out to obtain the velocity measurements (see figure 2*a*), which are needed to calculate the boundary layer flow in §3.

Note that before each experiment the glass surfaces of the wave tank and the vertical wall were thoroughly cleaned with a commercial cleaner. Then the tank was filled with fresh tap water, and the experiment was carried out immediately to avoid any possible free surface contamination. The equilibrium contact angle before each experiment was below 85°.

2.2. *Generation of solitary waves*

The solitary waves were generated using the method described by Goring (1979) with Grimshaw's (1971) third-order solution (for details see Liu *et al.* 2006). To generate two solitary waves for the head-on collision experiment, a solitary wave was first generated and allowed to reflect off the vertical glass wall installed at 20.75 m from the initial position of the wave maker paddle (see figure 2), and the second solitary wave was generated, which collided with the reflected wave at the desired location.

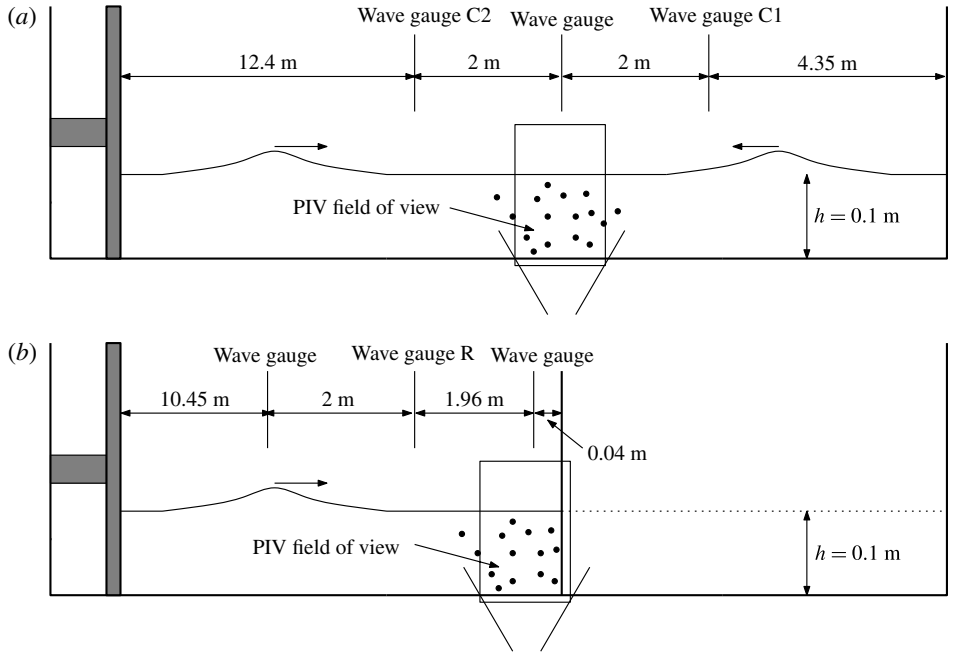

FIGURE 2. Experimental setup (not to scale) for (*a*) the head-on collision experiments and (*b*) the wall reflection experiments.

Here we only report the detailed experimental results for the solitary wave with wave height $H' = 1.1$ cm in water depth $h' = 10$ cm. Experiments with $H'/h' = 0.45$ were also carried out, which was the biggest solitary wave that could be generated in the wave flume. Although the formation of a small eddy was also observed in the large-amplitude case (see figure 1), only the smaller-amplitude case allows us to obtain an image of the vertical region between the still water level and the maximum elevation during the reflection in a single field of view (FOV), with a sufficiently high resolution to measure the boundary layer flow along the vertical wall.

The profiles of solitary waves measured at 2 m before the point of collision/reflection are shown in figure 3, in which η' denotes the water surface elevation, t' is the time coordinate, and t'_0 is the time when the crest of each solitary wave passes the respective wave gauge. Notice that the two colliding solitary waves in the collision experiment, measured at wave gauges C1 and C2, respectively, indeed have the same height, which is also very close to the one used in the reflection experiment, measured at gauge R (see figure 3). The measurements also show that the experimentally generated solitary waves agree very well with the fully nonlinear solution by Tanaka (1986) and the solution of the KdV equation.

2.3. *Quantitative flow visualization techniques*

The field of view (FOV) of the images was illuminated by a continuous argon ion laser (Coherent Innova 90-6). By passing the laser beam through a cylindrical lens, a light sheet was formed at 20 cm from the nearest sidewall. Two different sizes of FOV were used: the larger FOV (20 cm × 25 cm) was able to capture the entire water column at the moment of the highest elevation, while the smaller FOV (6.5 cm × 4.8 cm) was used to resolve the boundary layer flow along the vertical wall during the reflection.

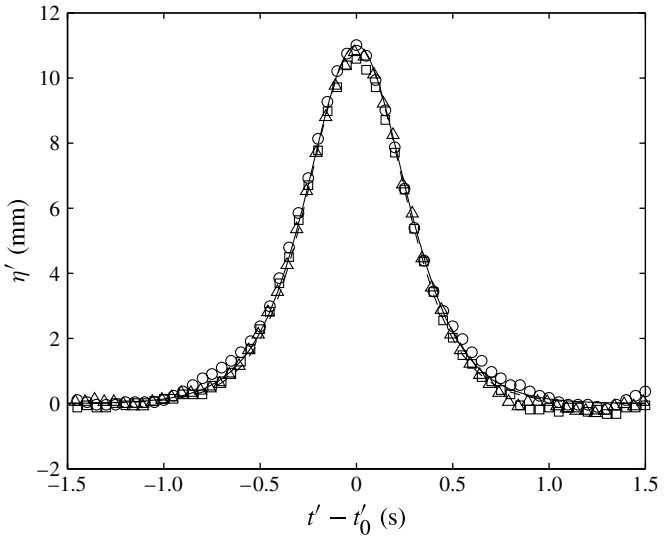

FIGURE 3. Solitary wave profiles measured at 2 m before the point of collision/reflection: ◯, measured data at wave gauge C1; △, measured data at wave gauge C2; □, measured data at wave gauge R; ——, fully nonlinear theory by Tanaka (1986); – – – – –, the solution of the KdV equation.

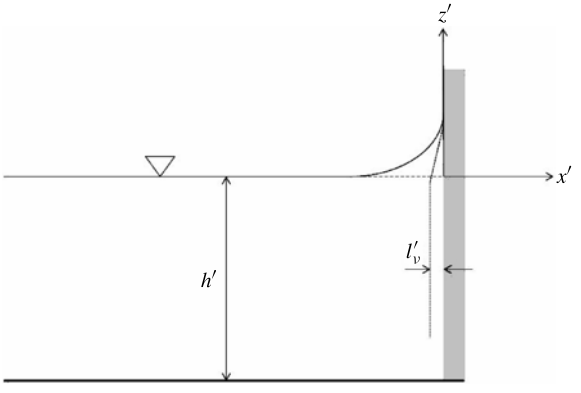

FIGURE 4. The coordinate system and the length scales that are used to non-dimensionalize the coordinates (not to scale).

The images were captured using a high-speed/high-resolution digital camera (vision research phantom V9.1, 1016 Hz at 1632 × 1200 pixels) at 250 Hz with 1 ms exposure.

With the images from the larger FOV, the velocity field data were obtained from the successive cross-correlation analyses of two neighbouring images with a square interrogation window (32 × 32 pixels) yielding a resolution of 5 mm in both directions. A more detailed description of the PIV technique can be found in Liu, Park & Cowen (2007). On the other hand, a PTV technique was used to extract the particle motions near the vertical wall from the images of the smaller FOV. For the PTV analysis, the software package DigiFlow (Dalziel 2008) was employed.

In addition, the free-surface profile was delineated in each image using the method suggested by Zarruk (2005). Due to the severe interference of the laser light in the meniscus, however, there is uncertainty of about ±5 pixels (=±0.1 mm) in determining the location of the contact line in the images of the smaller FOV. Therefore discussions of the contact line in the present paper must be understood from a macroscopic perspective.

3. Boundary layer flow along the vertical wall

As a solitary wave is reflected from a vertical wall, the vertical velocity near the wall scales with $\epsilon\sqrt{g'h'}$. The corresponding time scale may be determined by dividing the surface displacement of $O(H')$ by the vertical velocity scale, that is, $T' = H'/\epsilon\sqrt{g'h'} = h'/\sqrt{g'h'}$. Then the boundary layer thickness near the vertical wall can be estimated as $l'_v = \sqrt{\nu' T'}$. Using l'_v and h' as the horizontal and the vertical length scales, respectively, the scale of the horizontal velocity can be deduced from the continuity equation as $\epsilon\left(l'_v/h'\right)\sqrt{g'h'}$. The length scales and the coordinate system is depicted in figure 4. Note that the boundary layer thickness is much smaller than the water depth, i.e. $l'_v/h' \ll 1$, and that the horizontal velocity is one order smaller than the vertical velocity.

The dimensionless momentum equation in the vertical direction can be expressed as

$$\frac{\partial w}{\partial t} + \epsilon\left(u\frac{\partial w}{\partial x} + w\frac{\partial w}{\partial z}\right) = -\frac{\partial p_d}{\partial z} + \frac{\partial^2 w}{\partial x^2} + Re^{-1}\frac{\partial^2 w}{\partial z^2}, \tag{3.1}$$

where (x, z) are dimensionless horizontal and vertical coordinates, respectively, with the origin placed at the intersection of the still water level and the vertical wall, (u, w) are the corresponding dimensionless velocity components, t is the dimensionless time coordinate, $p_d = (p' + \rho' g' z')/\rho' g' H'$ is the dimensionless dynamic pressure, and $Re = h'\sqrt{g'h'}/\nu'$ is the Reynolds number. For a solitary wave with $\epsilon = 0.1$ in water depth $h' = 10$ cm, $Re^{-1} \approx 10^{-5}$. We remark here that the leading-order momentum equation in the horizontal direction results in uniform pressure across the boundary layer. Also, the boundary layer approach breaks down in the meniscus.

For small ϵ and Re^{-1}, we can linearize the boundary layer equation to obtain

$$\frac{\partial w}{\partial t} = -\frac{\partial p_d}{\partial z} + \frac{\partial^2 w}{\partial x^2}. \tag{3.2}$$

Note that even for highly nonlinear solitary waves such as the one in figure 1, (3.2) can still be applied as long as the wall boundary layer flow is uniform in the vertical direction (see figure 4 and the associated discussion in Liu *et al.* 2007).

Now, let $w = w_i + w_r$, where w_i is the inviscid free-stream velocity and satisfies

$$\frac{\partial w_i}{\partial t} = -\frac{\partial p_d}{\partial z}, \quad x = 0 \tag{3.3}$$

and w_r is the leading-order boundary layer correction. Thus, inside the boundary layer, we have

$$\frac{\partial w_r}{\partial t} = \frac{\partial^2 w_r}{\partial x^2}, \tag{3.4}$$

with the initial condition

$$w_r = 0, \quad t = -\infty, \tag{3.5}$$

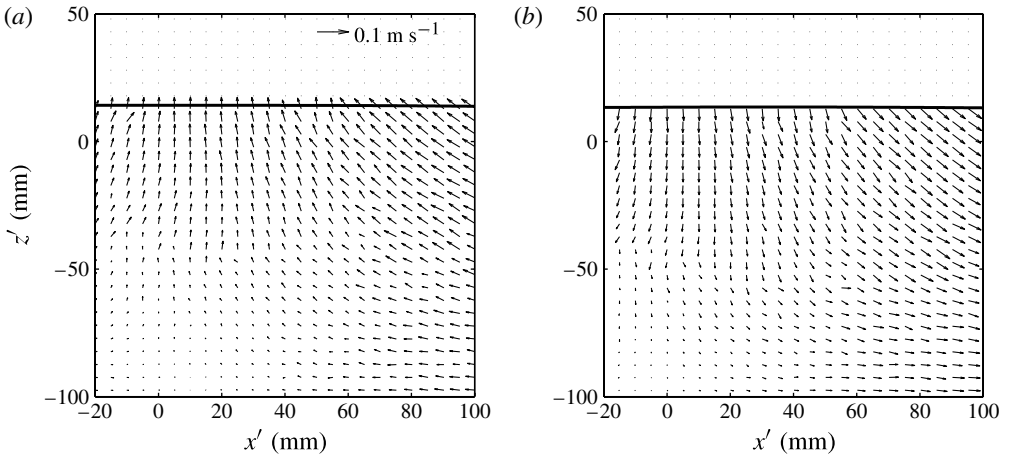

FIGURE 5. The velocity patterns obtained from the head-on collision of two identical solitary waves experiment: (*a*) $t = -1.6$, (*b*) $t = 1.8$, where the dimensionless time t is zero at the instant of the highest water surface displacement during the collision.

and the boundary conditions

$$w_r = -w_i, \quad x = 0, \quad w_r = 0, \quad x = -\infty. \tag{3.6}$$

The analytical solution for (3.4) with (3.5) and (3.6) is (Butkovsky 1982)

$$w_r = \frac{x}{\sqrt{4\pi}} \int_{-\infty}^{t} \frac{w_i}{(t-s)^{3/2}} \mathrm{e}^{-x^2/4(t-s)} \, \mathrm{d}s. \tag{3.7}$$

In the following, we shall report experimental measurements of the boundary layer flow along the vertical wall during the solitary wave reflection process. The analytical solution (3.7) will be compared with the experimental result.

3.1. *The free-stream velocity*

In calculating the analytical solution for w_r in (3.7), we need information on the free-stream velocity w_i, which can be experimentally obtained from the head-on collision experiment, since the collision of two identical solitary waves is equivalent to the reflection of a solitary wave from a vertical wall without effects of wall boundary layer and the contact line at the wall.

Typical velocity patterns from the PIV analysis of head-on collision experiments are shown in figure 5. One can clearly observe that the vertical velocity near the free surface at the line of symmetry ($x' = 0$) is more or less uniform, and its magnitude is comparable to that of the horizontal velocity in the region far from the line of symmetry.

Figure 6 shows the time series of the vertical velocity at the line of symmetry near the still water level during the head-on collision of two identical solitary waves experiment. The flow is essentially uniform between $z = -0.2$ and $z = -0.1$, and the least-squares-fitted curve, using the Fourier sine series with the first four terms, is taken as the free-stream velocity to be used to calculate the theoretical solution (3.7). Note that the origin of the dimensionless time coordinate is set at the instant when w_i crosses zero, which corresponds to the highest water surface elevation. Further, we remark that the free-stream velocity data are available only up to $t \approx 5$.

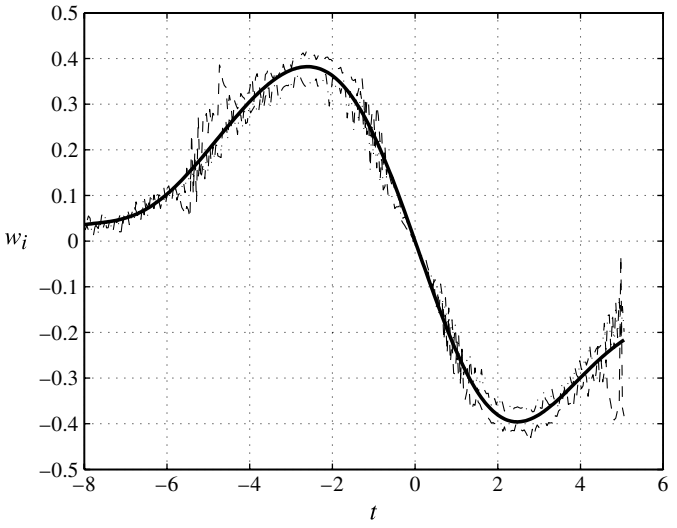

FIGURE 6. The time series of the dimensionless vertical velocity along the line of symmetry near the initial free surface: —·—, $z = -0.2$; – – – –, $z = -0.1$; ——, the least-squares-fitted curve using the data between $-0.2 \leqslant z \leqslant -0.1$.

Particle number	x	z	Symbols in figures 7–9
1	−6.55	−0.15	◯
2	−5.26	−0.15	△
3	−3.74	−0.14	□
4	−3.16	−0.14	▽
5	−1.87	−0.11	+
6	−1.75	−0.16	×

TABLE 1. Initial dimensionless coordinates of the six particles of which the trajectories are traced in figure 7. The particles are numbered in such a way that particle 1 is the farthest from the wall and particle 6 is the nearest.

3.2. *The boundary layer flow*

The boundary layer flow along the vertical wall was measured by tracking individual seeding particles. To illustrate, six particles were chosen, which were initially located near the wall ∼1.5 cm below the still water level (table 1). Vertical and horizontal trajectories of the six particles, whose initial locations are given in table 1, are shown in figure 7. As expected, the horizontal displacements are negligible compared to the vertical counterparts near the vertical wall.

Now the Lagrangian velocity of each particle in table 1 can be obtained by taking the time derivative of each trajectory. As implied in (3.1), the change in the vertical direction (i.e. $\partial/\partial z$) within the boundary layer is smaller than in the horizontal direction (i.e. $\partial/\partial x$). Hence one may assume that the vertical component of the boundary layer flow is uniform along the wall within the displacement of the particles in table 1 as long as they are not very near the meniscus or the stagnation point at the bottom corner. Then the Lagrangian velocity can be compared with the theoretical solution (3.7) that is obtained in the Eulerian reference frame. Figure 8 shows the

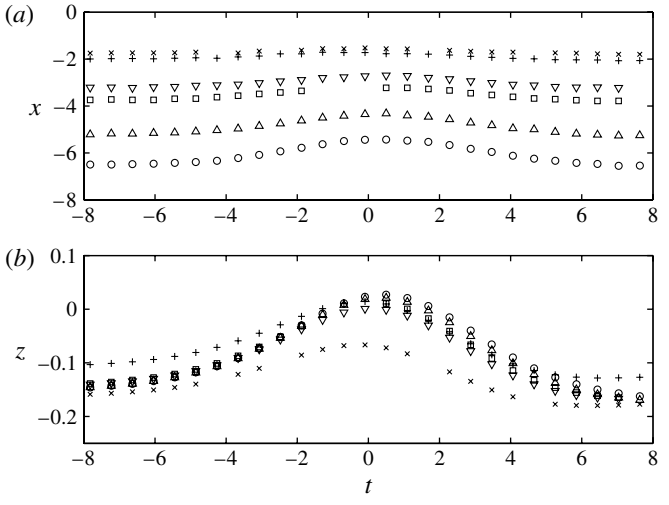

FIGURE 7. Dimensionless trajectories of the six particles listed in table 1: (*a*) the horizontal trajectories; (*b*) the vertical trajectories. Only every fifteenth data point is plotted. Note that the horizontal displacements are normalized by $l'_v = 0.3$ mm and the vertical ones by $h' = 10$ cm, and that $l'_v \ll h'$.

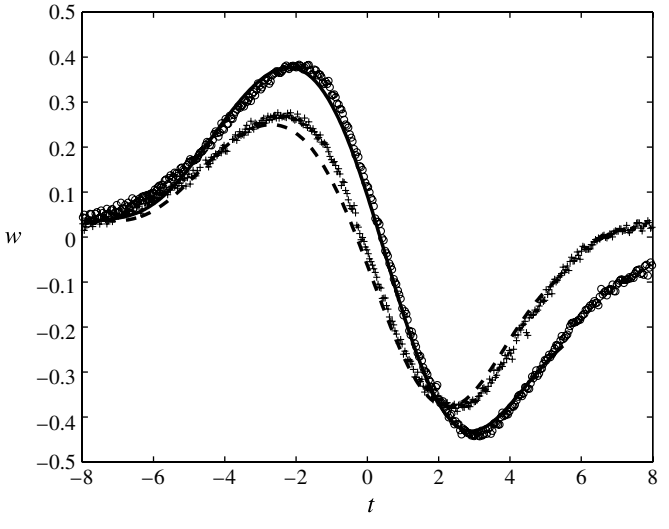

FIGURE 8. The time series of the dimensionless vertical velocity near the wall during the solitary wave reflection process: ◯, PTV data of particle 1 in table 1; +, PTV data of particle 5; ——, the theoretical solution with w_r given by (3.7) at the initial horizontal location of particle 1; – – – – –, the theoretical solution at the initial horizontal location of particle 5. Note that the velocity for particle 5, which is closer to the vertical wall, becomes positive during the last phase of the solitary wave reflection process ($t \approx 7$).

time history of the vertical component of the Lagrangian velocity for the two particles (1 and 5) compared with the theoretical Eulerian velocity. Despite the fact that several simplifying approximations have been adopted in the theory, the agreement between

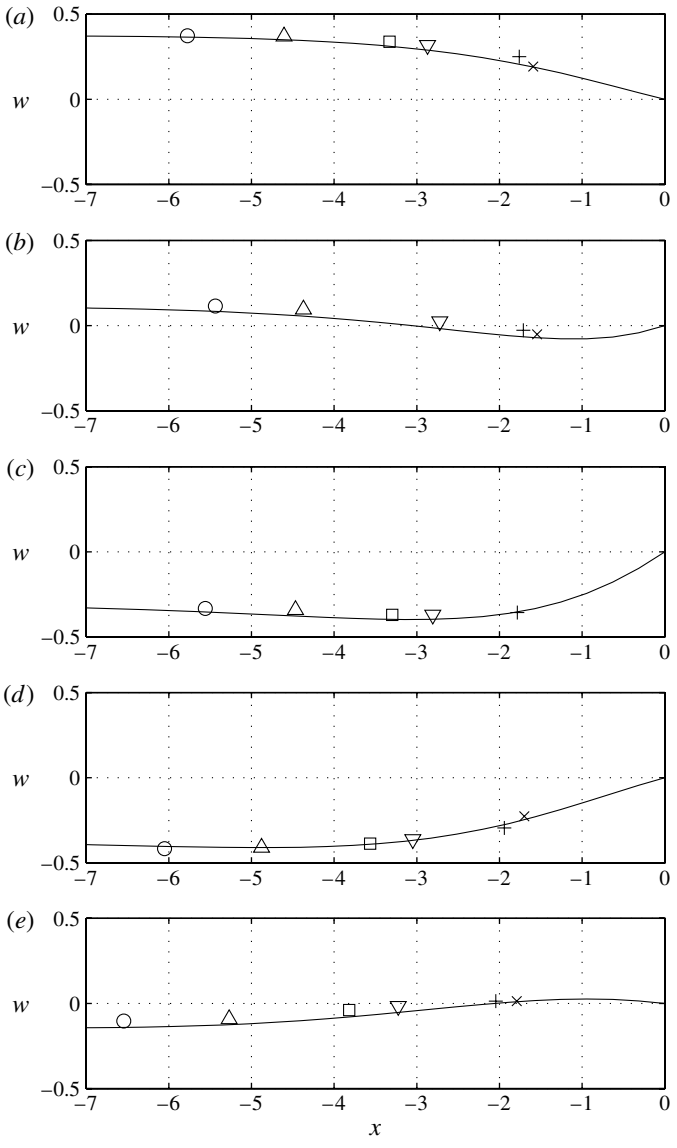

FIGURE 9. The horizontal profiles of the dimensionless vertical velocity near the wall during the solitary wave reflection process: symbols, PTV data of the particles listed in table 1; ——, the theoretical solution (3.7). (*a*) $t = -1.80$; (*b*) $t = -0.02$; (*c*) $t = 1.81$; (*d*) $t = 3.67$; (*e*) $t = 7.00$. Note that the theoretical solution in (*e*) was calculated using the velocity of particle 1 as the free-stream velocity, as the data from the head-on collision experiment is not available for $t > 5$.

the experimental data and the theoretical prediction is very good. Also note that the theoretical solution is calculated only up to $t \approx 5$, beyond which the free-stream velocity is not available.

Excellent agreement can also be demonstrated in the snapshots of the horizontal profiles of the vertical velocity (figure 9). We remark here that the boundary layer flow near the wall changes its direction from moving upwards to downwards sooner

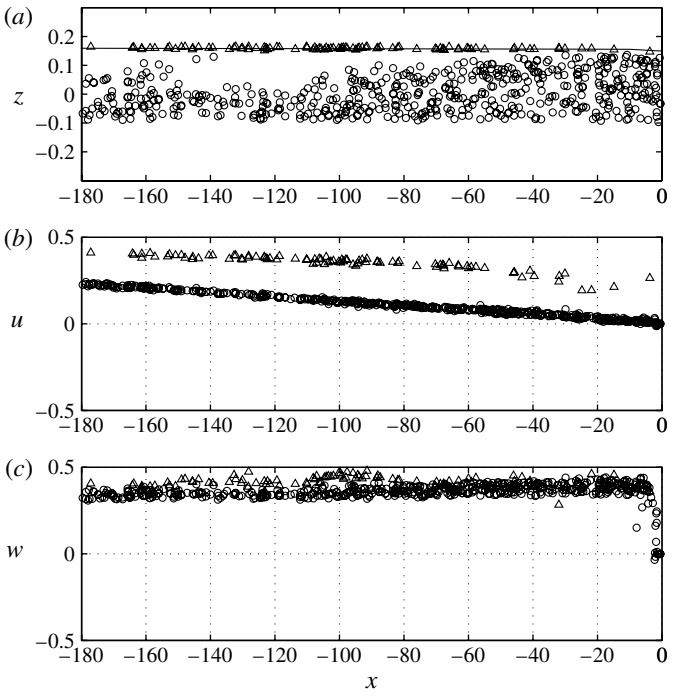

FIGURE 10. Dimensionless particle velocities on and near the free surface during the ascending phase at $t = -1.53$: ——, the free-surface profile; △, particles on the free surface; ◯, particles below the free surface. (*a*) Locations of PTV data; (*b*) horizontal components of particle velocities as a function of x; (*c*) vertical components of particle velocities as a function of x.

than the free-stream flow does (see figure 9*b*). The boundary layer flow near the wall reverses its direction once again near the end of the reflection process ($t \approx 7$), as can be seen in figures 8 and 9(*e*).

4. Flows near the moving contact line

4.1. *Rolling motion of the free surface*

In addition to the development of boundary layer flows, another important wall effect can be revealed by observing particle velocities on the free surface. Figures 10 and 11 show the typical velocity data during the ascending and descending phases, respectively. Figures 10(*a*) and 11(*a*) are snapshots of particle locations on and below the free surface, where PTV velocity data are obtained, and panels (*b*) and (*c*) of each figure are the corresponding horizontal and vertical velocity components of the same particles identified in panel (*a*), plotted against the horizontal coordinate.

While the PTV particles denoted by the circles in the first panels spread over 3 cm in the vertical direction, the circles in figure 10(*b*,*c*) collapse into a single line, indicating that the velocity field just below the free surface is uniform in the vertical direction. On the other hand, the horizontal component of particle velocity on the surface is noticeably different from the ones below the surface, resulting in a strong horizontal shear that is apparently much more significant than one would expect in the free-surface boundary layer. We did not observe this strong shear in the

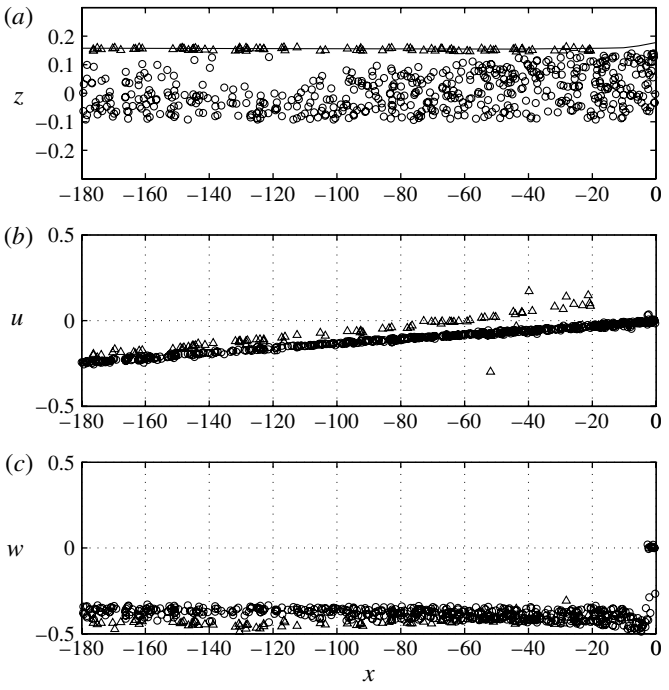

FIGURE 11. Dimensionless particle velocities on and near the free surface during the descending phase at $t = 2.45$: ——, the free-surface profile; △, particles on the free surface; ◯, particles below the free surface. (*a*) Locations of PTV data; (*b*) horizontal components of particle velocities as a function of x; (*c*) vertical components of particle velocities as a function of x.

head-on collision experiments, and we maintain that the shear is not due to surface contamination.

During the ascending phase (figure 10), the particles on the free surface approach the wall much faster than those in the water body, implying that the wetting of the wall is mainly contributed by the water particles on the free surface. In other words, the free surface attaches itself to the vertical wall and the particles on the free surface are pulled into the wall as if they were on a conveyor belt. This free-surface motion is consistent with the surface rolling motion that was observed by Dussan & Davis (1974). Furthermore, even in the descending phase (figure 11), the particles on the free surface first move toward the wall, which is in the opposite direction from that of the horizontal velocity below the free surface, and change their direction only at the end of the reflection process. To the authors' knowledge, ours is the first measurement of the surface rolling in which the velocity and the displacement of the contact point are large enough for the contact angle to change from an acute angle to an obtuse angle and back to an acute angle.

We emphasize here again that, in the head-on collision experiments, both the horizontal and the vertical velocity components were uniform in the vertical direction near and on the free surface.

4.2. *The contact angle*

Due to multiple reflections and refraction of the laser light, it is difficult to accurately identify the contact line location and the contact angle from PTV images. When

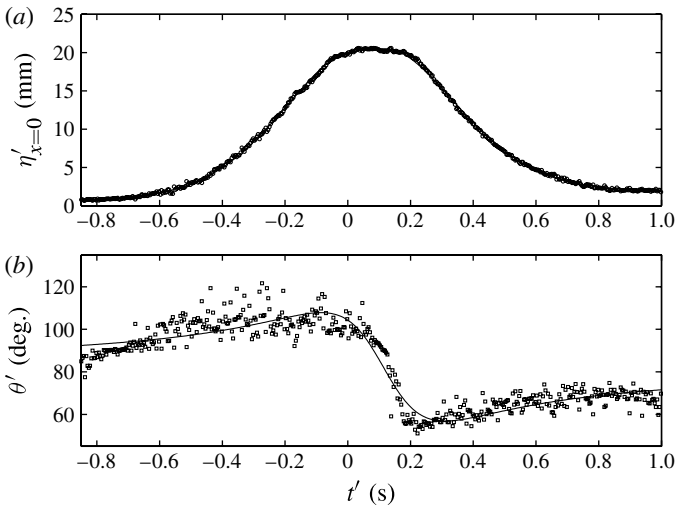

FIGURE 12. Contact line motions. (*a*) ◯, the time series of measured vertical locations of the contact line; ——, a fitted curve using a sum of three Gaussian functions. (*b*) □, the time series of the measured contact angle in degrees; ——, a fitted curve using a ratio of two second-degree polynomials.

locating the contact line in each image, there was an uncertainty of ±5 pixels or ±0.1 mm in both x'- and z'-directions. Figure 12(*a*) shows a time series of measured vertical locations of the contact line. A fitted curve, consisting of a sum of three Gaussian functions with the coefficient of determination being 0.999, is also plotted.

The macroscopic contact angle was measured by approximating the free surface near the contact line by a straight line between the contact point and the nearest identifiable point on the free surface, where the distance between the two points are on average ∼2 mm. During the ascending phase of contact line motion, the free surface is a concave curve, hence the macroscopic contact angle tends to be underestimated. Similarly we must have overestimated the contact angle during the descending phase due to the convex free surface. The results are shown in figure 12(*b*), where θ' is the macroscopic contact angle in degrees. While the contact angle data exhibit relatively larger errors (figure 12*b*), it appears that data scattering is smaller during the descending phase. Again the data are fitted by a curve using a ratio of two second-degree polynomials with the coefficient of determination being 0.91. As the wave arrives at the wall, the contact angle gradually increases from below 85 to ∼110°. While the contact line lingers at the highest elevation, one can see the rapid decrease of the contact angle. Then it gradually increases as the wave propagates away from the wall.

The contact line velocity is estimated by taking the time derivative of the fitted curve in figure 12(*a*), and is shown in figure 13. Also plotted is the free-stream velocity, which was taken from the vertical velocity at the line of symmetry and near the still water level during the head-on collision experiment (see figure 6). It is interesting to note that the speed of the moving contact line has a larger amplitude than the free-stream velocity. We also notice that the contact line stands still at the highest elevation for ∼0.1 s.

As discussed in § 1, previous theoretical studies predict that under steady flow conditions the macroscopic contact angle is a simple function of the speed of the moving contact line. Since no such theory is known for unsteady flows with high

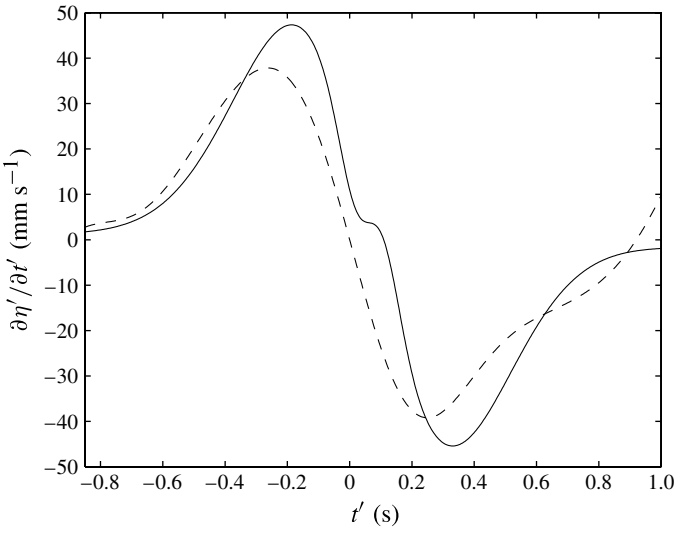

FIGURE 13. The velocity of the moving contact line: ——, the time derivative of the fitted curve in figure 12(*a*); – – – – –, the free-stream velocity shown in figure 6.

Reynolds numbers, we compare our results with the model suggested by Hocking (1987*b*) (see figure 14), that is,

$$\frac{\partial \eta'}{\partial t'} = \begin{cases} \lambda'_a \left(-\dfrac{\partial \eta'}{\partial x'} - \alpha'_a \right) & \text{if } -\dfrac{\partial \eta'}{\partial x'} > \alpha'_a, \\ \lambda'_r \left(-\dfrac{\partial \eta'}{\partial x'} - \alpha'_r \right) & \text{if } -\dfrac{\partial \eta'}{\partial x'} < \alpha'_r, \end{cases} \tag{4.1}$$

where

$$\frac{\partial \eta'}{\partial x'} = \tan(90^\circ - \theta'). \tag{4.2}$$

Note that, in plotting figure 14, the contact angle data are taken from the fitted curve in figure 12(*b*).

It is remarkable that Hocking's (1987*b*) model (4.1) works very well when the moving contact line has positive acceleration. Considering that the contact angle is underestimated in the ascending phase and overestimated in the descending phase, λ'_a is indeed overestimated, while λ'_r is underestimated, therefore $\lambda'_a \approx \lambda'_r \approx 0.2$ m s^{-1}. On the other hand, the model fails to capture the hysteretic behaviour during the deceleration of the contact line.

4.3. *The capillary wave at the highest elevation of the free surface*

Another interesting observation is the generation of capillary waves when the contact line reaches its highest elevation and the contact angle rapidly decreases (figure 15). In figure 15, the wavelength and the wave period are estimated to be 1 cm and 49 ms, respectively, from the distributions of the vertical surface velocity at two closely spaced times. The dispersion relation for capillary waves is

$$\omega'^2 = \frac{\sigma'}{\rho'} k'^3, \tag{4.3}$$

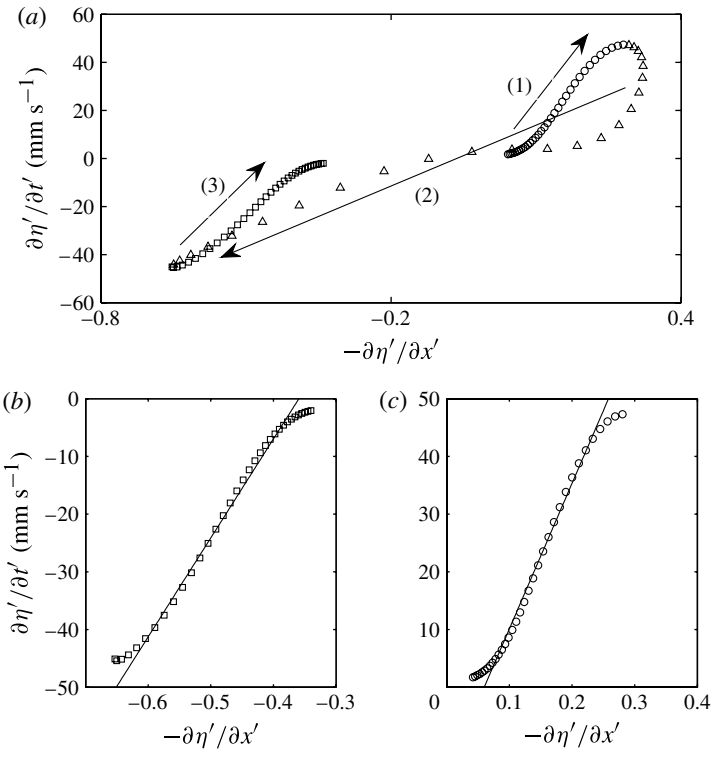

FIGURE 14. Plot of the rise velocity of contact line versus the contact angle. (*a*) ◯, the experimental data for $\partial^2\eta'/\partial t'^2 > 0$ and $\partial\eta'/\partial t' > 0$; △, $\partial^2\eta'/\partial t'^2 < 0$; □, $\partial^2\eta'/\partial t'^2 > 0$ and $\partial\eta'/\partial t' < 0$; the arrows denote the time evolution and are numbered in the order of time. (*b*) □, the same as in (*a*); ——, a fitted linear line with $\lambda_r' = 0.17$ m s^{-1} and $\alpha_r' = -0.36$ in (4.1). (*c*) ◯, the same as in (*a*); ——, a fitted linear line with $\lambda_a' = 0.25$ m s^{-1} and $\alpha_a' = 0.06$ in (4.1). The coefficients of determination for the fitted lines in (*b*,*c*) are both 0.98.

in which ω' is the wave frequency and k' is the wavenumber. For a 1 cm wavelength, (4.3) yields a wave period of 48 ms, which is very close to the observation. If it were a gravity wave, the deep-water dispersion relation ($\omega'^2 = g'k'$) would have given 80 ms for the wave period. These capillary waves are dissipated within five wavelengths. As the contact line starts to descend, no more capillary waves are generated.

4.4. *Trajectories of the particles near the moving contact line*

So far, we have presented our observations of the flow field near the moving contact line. The flow field is highly complex, as the wall boundary layer flow, the flow induced by the surface rolling motion, the change of the contact angle and the surface disturbance in the form of capillary waves all interact with one another in this region. To illustrate the effects of the interaction, we have tracked trajectories of a few seeding particles near the moving contact line (figures 16 and 17).

In figure 16, eight particles, which were initially located near the meniscus, have been tracked during the reflection of the solitary wave. It is noted that one of the particles (marked by ◯) travels from the free-stream region, passing through the meniscus about the instant of the highest elevation of the moving contact line, and finally to the wall boundary layer, which suggests that the free-stream region and the

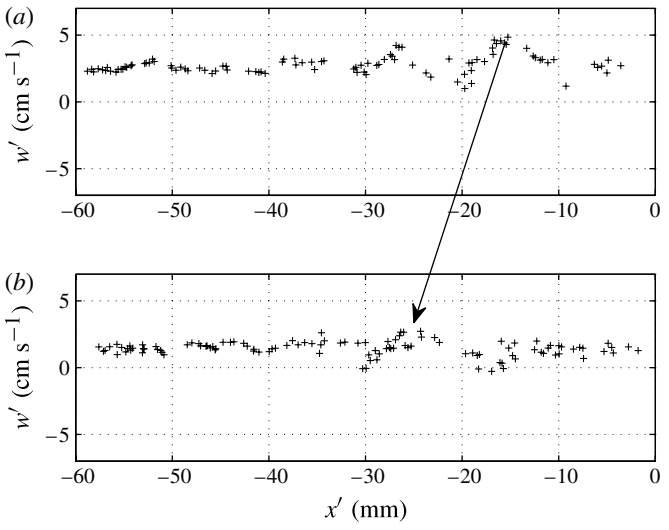

FIGURE 15. Vertical velocity at the free surface versus x' at two times during the reflection process: (*a*) $t = -0.49$; (*b*) $t = -0.06$. The time lapse between (*a*) and (*b*) is 44 ms, during which the waves travel by 0.9 cm, yielding a phase velocity of 20.45 cm s^{-1}. The wavelength is ∼1 cm and therefore the wave period is ∼49 ms.

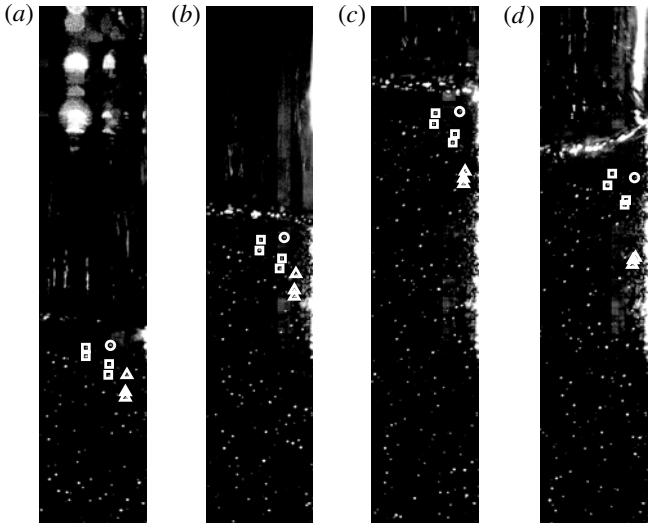

FIGURE 16. Snapshots of the raw PTV images. Eight particles which were initially near the meniscus are tracked and marked with symbols: □, the particles that remain in the free-stream region; △, the particles that remain in the wall boundary layer; ◯, the particle that was initially in the free-stream region and was later entrained in the wall boundary layer. (*a*) $t = -4.93$; (*b*) $t = -2.47$; (*c*) $t = -0.02$; (*d*) $t = 2.48$.

wall boundary layer communicate through the meniscus. We remark here that Mei & Liu (1973) used an order-of-magnitude analysis to demonstrate that the meniscus serves as a channel of energy flow from the core of the fluid flow to the sidewall

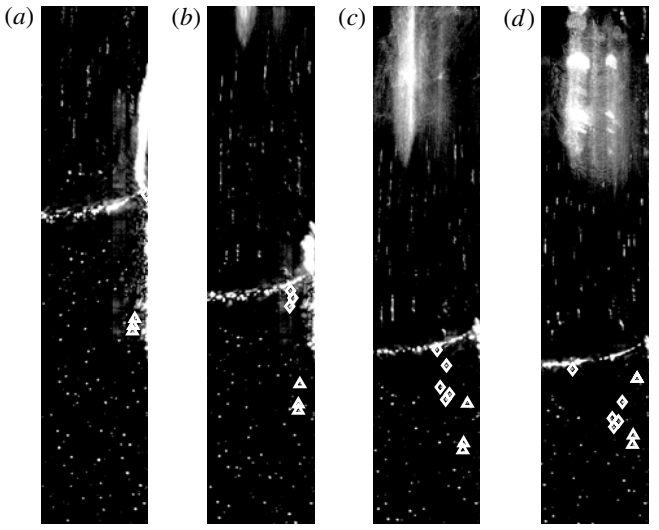

FIGURE 17. Snapshots of the raw PTV images: △, the same particles that were in the wall boundary layer in figure 16; ⋄, the particles identified as the jet ejecting from the moving contact line to the water body below. (*a*) $t = 3.43$, the first particle of the jet is seen at the contact line; (*b*) $t = 4.98$, the earlier part of the jet leaves the meniscus for the free-stream region; (*c*) $t = 7.43$, a particle of the later part of the jet is entrained in the surface boundary layer flow; (*d*) $t = 9.93$, another particle of the later part of the jet is entrained in the wall boundary layer flow, while a particle that belonged to wall boundary layer is being entrained to surface boundary layer flow.

boundary layer. Although their analysis was not complete, in the sense that it did not include surface tension which might contribute to wave damping (Hocking 1987*a*), it was the first theoretical attempt to point out the interaction between surface dynamics and wall boundary layer flows.

In the middle of the descending phase of the solitary wave reflection, a number of particles are seen to be ejected from the moving contact line down into the water body (figure 17). While the earlier part of the jet penetrates into the free-stream region, the particles that eject later are entrained to the surface boundary layer or to the wall boundary layer. Furthermore, one of the particles in the wall boundary layer is observed to be entrained in the surface boundary layer flow at the end of the reflection. Again, the meniscus seems to be the communication hub that connects the free-stream region and the two boundary layers.

To summarize the above discussion, pathlines and trajectories of some of the tracked particles are plotted in figures 18 and 19, respectively.

4.5. *Formation of the eddy left behind the reflected wave*

In § 4.4 it has been clearly shown that a jet is formed during the descending phase of the solitary wave reflection. In this subsection, we look for an explanation by combining all the observations we have reported in the present paper (see figure 20).

Figure 20(*b*) plots the horizontal velocity of the particle on the free surface at the moving contact line. To obtain these values, it was first noted that the horizontal velocities, both on the free surface and below the free surface, when plotted against the horizontal coordinate can be approximated by a straight line, as can be seen in

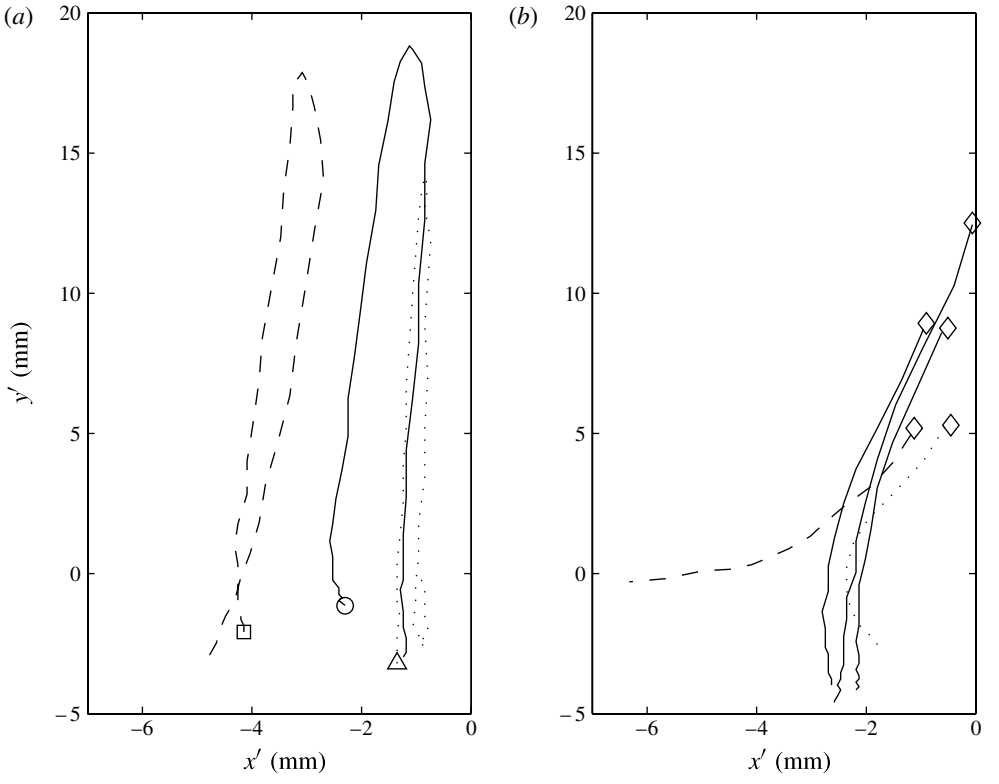

FIGURE 18. The pathlines of the particles tracked in figures 16 and 17. Each pathline starts from the location marked with the respective symbol: □, one of the particles that remained in the free-stream region; △, the particle that was in the wall boundary layer and entrained in the surface boundary layer at the end of the reflection process; ◯, the particle that was initially in the free-stream region and was later entrained in the wall boundary layer; ◇, the particles of the jet ejected from the moving contact line.

figures 10 and 11. The values were then taken at the intersection of the line with $x' = 0$. With this velocity as the boundary condition, the flow induced by the surface rolling motion has been calculated using the similar procedure described in § 3 and integrated along the z'-coordinate to obtain the curve in figure 20(*c*). Also shown in the same panel is the rotational component of the wall boundary layer flow (w'_r) integrated along the x'-coordinate.

The reflection process can be divided into seven regimes.

I ($t' < -0.6$ s; $t < -6$). As the wave arrives, the wall boundary layer starts to develop. The contact line lags behind the free-stream velocity near the centreline, which compensates for the flow deficit due to the wall boundary layer near the meniscus. The lag of the moving contact line also contributes to the increase of the contact angle, or equivalently, the expansion of the meniscus.

II ($-0.6 < t' < -0.2$ s; $-6 < t < -2$). The contact angle reaches its maximum and maintains it. As the free-stream flow accelerates, so does the speed of the moving contact line. This in turn induces increasing horizontal velocity at the contact line. This in-flow contributes to the further upward motion of the contact line, and its speed overtakes that of the free-stream flow. The flow deficit in the wall boundary layer near

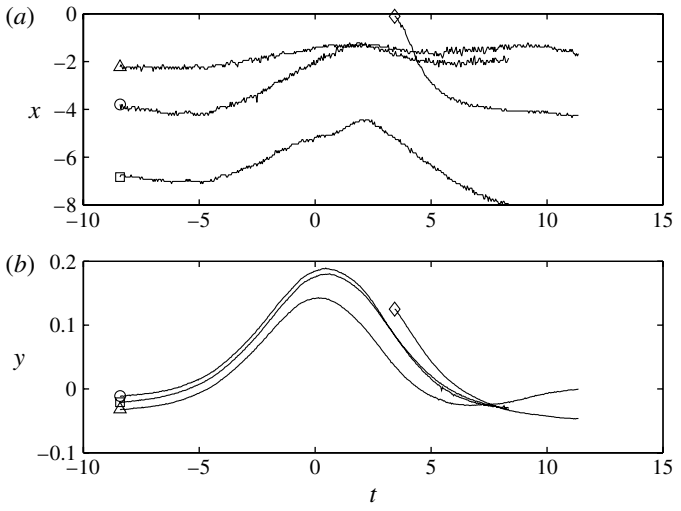

FIGURE 19. Dimensionless trajectories of the particles in figure 18(*a*) and the first particle of the jet in figure 18(*b*): (*a*) the horizontal trajectories; (*b*) the vertical trajectories. Note that the horizontal displacements are normalized by $l'_v = 0.3$ mm and the vertical by $h' = 10$ cm, and that $l'_v \ll h'$.

the meniscus is also compensated by the horizontal in-flow due to the surface rolling motion.

III ($-0.2 < t' < 0$ s; $-2 < t < 0$). The free-stream velocity decelerates to zero, which induces deceleration of the contact line and the horizontal velocity on the free surface. Though the horizontal in-flow at the contact line is still positive, the flow deficit in the wall boundary layer attains its peak during this period and the horizontal in-flow does not seem to be enough to cover this deficit. Instead, some flow is drawn from the meniscus, resulting in faster deceleration of the contact line compared to the free-stream velocity. This sudden deceleration of the contact line motion is accompanied by noticeable capillary waves on the free surface, which propagate away from the wall. No significant change in the contact angle is observed.

IV ($0 < t' < 0.1$ s; $0 < t < 1$). The contact line maintains a more or less fixed location at its maximum elevation while the free-stream velocity starts to accelerate (in a downward direction). The rolling-motion-induced horizontal velocity at the contact line decreases to zero, but the in-flow during this period seems to balance with the decreasing flow deficit in the wall boundary layer. The contact angle decreases to become almost horizontal. The PTV particle marked by ◯ in figures 16, 18 and 19 is transported from the free-stream region to the wall boundary layer during this period.

V ($0.1 < t' < 0.2$ s; $1 < t < 2$). As the wave reflects away from the wall, the contact angle rapidly decreases and the meniscus shrinks. The contact line also accelerates in a downward direction, which induces the rolling motion of the free surface again. This positive horizontal flow due to the rolling motion seems to compensate the flow deficit in the wall boundary layer.

VI ($0.2 < t' < 0.35$ s; $2 < t < 3.5$). The wall boundary layer flow changes sign and directs upward, while the negative vertical velocity of the moving contact line and the positive horizontal velocity at the contact line keeps accelerating. At the end of this period, when the horizontal velocity is at its peak, the in-flow due to the surface

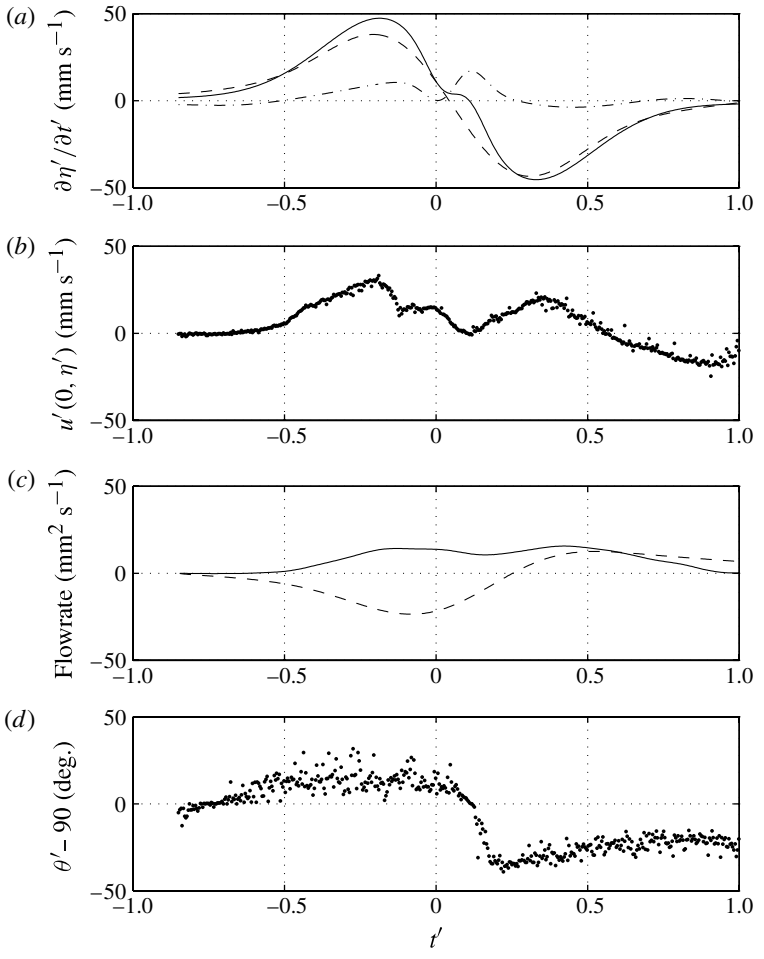

FIGURE 20. The time histories of the experimental data. (*a*) ——, the speed of the moving contact line, i.e. the time derivative of the fitted curve in figure 12(*a*); – – – – –, PTV data of particle 1 in table 1, which was used as the free-stream velocity to plot figure 9(*e*); —·—, the difference between the two. (*b*) •, the horizontal velocity of the particle on the free surface at the contact line. (*c*) ——, the flowrate due to the free-surface velocity in (*b*), i.e. $\int u'(0,z')\,\mathrm{d}z'$; – – – – –, the deficit in flowrate in the wall boundary layer away from the meniscus, i.e. $\int w_r'(x')\,\mathrm{d}x'$. (*d*) The contact angle measured from the horizontal.

rolling motion that enters the meniscus cannot exit through the wall boundary layer, but bursts into the free-stream region, forming the jet. The contact angle gradually increases with almost the same rate in phase I.

VII ($t' > 0.35$ s; $t > 3.5$). As the positive wall boundary layer flow and the positive surface-rolling-induced flow continue, the jet is maintained, though its strength decreases and the particles that form the jet in this later period get entrained either in the wall boundary layer or the free-surface boundary layer. These entrainments are seen to be the eddy that was observed in § 1. Eventually the horizontal velocity at the contact line changes its direction and the particles that were originally in the wall boundary layer are observed to be entrained to the free-surface boundary layer.

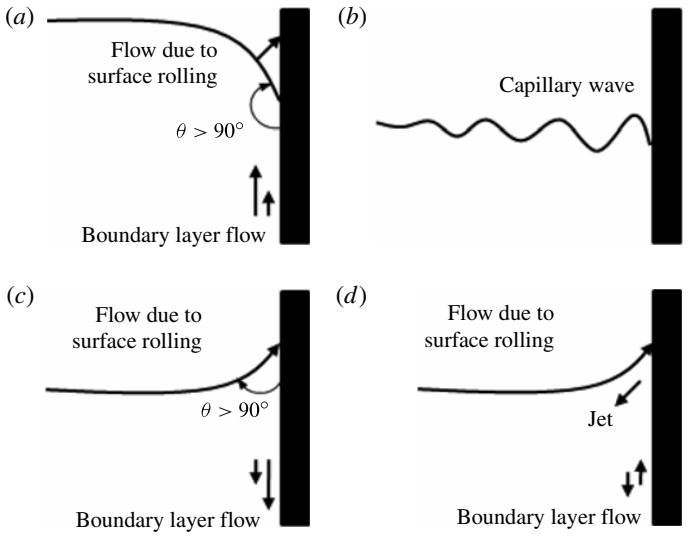

FIGURE 21. The interactions between the flow induced by the moving contact line and the wall boundary layer flow. (*a*) Incoming wave ($t < 0$); (*b*) the instant of highest elevation ($t \approx 0$); (*c*) outgoing wave ($t > 0$); (*d*) collision of boundary layer flow and surface-rolling-induced flow ($t > 3.5$).

To summarize these complex processes, a sketch is provided in figure 21.

Also, a movie that shows the formation of the jet as well as the induced anticlockwise eddy is available as the supplementary material to this paper at journals.cambridge.org/flm. Note that to reduce the file size we only include every fifth frame in the movie, and it is ten times as slow as real time. At the frame in which the jet is formed, the red half-circle in the movie indicates the locations of the jet.

5. Concluding remarks

In this paper we have reported a set of solitary wave reflection experiments illustrating the interactions between the free-surface motion and the wall boundary layer flow in the vicinity of the moving contact line.

As Dussan & Davis (1974) pointed out, the surface rolling motion as well as the wall boundary layer flow is the consequence of the no-slip boundary condition at the wall. However, the inertia and the dynamically changing contact angle create a lag between the two flows. This lag causes remarkable features, especially during the deceleration of the free-stream flow. For example, during the deceleration in the ascending phase of the wave reflection, the increase in the flow deficit in the wall boundary layer flow drains some water from the meniscus, which is accompanied by relatively large-amplitude capillary waves. Later, when the free-stream flow again decelerates in its descending phase, both the surface-rolling-induced surface flow and the wall boundary layer flow direct toward the contact line, which gives rise to the formation of the jet.

Another important observation is that the fluid particles in different regions such as the free stream, the free-surface boundary layer and the wall boundary layer can be transported to other regions by passing through the meniscus.

This work provides a way to couple the dynamics of the contact line to large-scale flow at high Reynolds numbers, which could be crucial in many industrial

and environmental flow problems involving sloshing of a bounded liquid with a free surface.

Acknowledgements

This work has been supported by grants from the National Science Foundation to Cornell University. Y.S.P. acknowledges financial support from the Royal Academy of Engineering through a Newton International Fellowship.

Supplementary data

Supplementary data are available at journals.cambridge.org/flm.

REFERENCES

BUTKOVSKY, A. G. 1982 *Green's Functions and Transfer Functions Handbook*. Halsted Press/Wiley.

BYATT-SMITH, J. G. B. 1988 The reflection of a solitary wave by a vertical wall. *J. Fluid Mech.* **197**, 503–521.

BYATT-SMITH, J. G. B. 1989 The head-on interaction of two solitary waves of unequal amplitude. *J. Fluid Mech.* **205**, 573–579.

CHAN, R. K.-C. & STREET, R. L. 1970 A computer study of finite-amplitude water waves. *J. Comput. Phys.* **6**, 68–94.

COOKER, M. J., WEIDMAN, P. D. & BALE, D. S. 1997 Reflection of a high-amplitude solitary wave at a vertical wall. *J. Fluid Mech.* **342**, 141–158.

COX, R. G. 1998 Inertial and viscous effects on dynamic contact angles. *J. Fluid Mech.* **357**, 249–278.

CRAIG, W., GUYENNE, P., HAMMACK, J., HENDERSON, D. & SULEM, C. 2006 Solitary wave interactions. *Phys. Fluids* **18**, 057106.

DALZIEL, S. B. 2008 Digiflow user guide. http://www.dalzielresearch.com/digiflow/.

DUSSAN V, E. B. 1979 On the spreading of liquids on solid surfaces: static and dynamic contact lines. *Annu. Rev. Fluid Mech.* **11**, 371–400.

DUSSAN V, E. B. & DAVIS, S. H. 1974 On the motion of a fluid–fluid interface along a solid surface. *J. Fluid Mech.* **65**, 71–95.

EGGERS, J. & STONE, H. A. 2004 Characteristic lengths at moving contact lines for a perfectly wetting fluid: the influence of speed on the dynamic contact angle. *J. Fluid Mech.* **505**, 309–321.

GORING, D. K. 1979 Tsunamis: the propagation of long waves onto a shelf. PhD dissertation, California Institute of Technology.

GRIMSHAW, R. 1971 The solitary wave in water of variable depth. Part 2. *J. Fluid Mech.* **46**, 611–622.

HOCKING, L. M. 1987*a* The damping of capillary–gravity waves at a rigid boundary. *J. Fluid Mech.* **179**, 253–266.

HOCKING, L. M. 1987*b* Waves produced by a vertically oscillating plate. *J. Fluid Mech.* **179**, 267–281.

HOCKING, L. M. 1987*c* Reflection of capillary–gravity waves. *Wave Motion* **9**, 217–226.

HOCKING, L. M. & DAVIS, S. H. 2002 Inertial effects in time-dependent motion of thin films and drops. *J. Fluid Mech.* **467**, 1–17.

LIU, P. L.-F., PARK, Y. S. & COWEN, E. A. 2007 Boundary layer flow and bed shear stress under a solitary wave. *J. Fluid Mech.* **574**, 449–463.

LIU, P. L.-F., SIMARRO, G., VANDEVER, J. & ORFILA, A. 2006 Experimental and numerical investigation of viscous effects on solitary wave propagation in a wave tank. *Coast. Engng* **53**, 181–190.

MAXWORTHY, T. 1976 Experiments on collisions between solitary waves. *J. Fluid Mech.* **76**, 177–185.

McHUGH, J. P. & WATT, D. W. 1998 Surface waves impinging on a vertical wall. *Phys. Fluids* **10**, 324–326.

MEI, C. C. & LIU, P. L.-F. 1973 The damping of surface gravity waves in a bounded liquid. *J. Fluid Mech.* **59**, 239–256.

MILES, J. 1990 Capillary-viscous forcing of surface waves. *J. Fluid Mech.* **219**, 635–646.

NGAN, C. G. & DUSSAN, V. E. B. 1982 On the nature of the dynamic contact angle: an experimental study. *J. Fluid Mech.* **118**, 27–40.

SU, C. H. & MIRIE, R. M. 1980 On head-on collisions between two solitary waves. *J. Fluid Mech.* **98**, 509–525.

TANAKA, M. 1986 The stability of solitary waves. *Phys. Fluids* **29**, 650–655.

TING, C.-L. & PERLIN, M. 1995 Boundary conditions in the vicinity of the contact line at a vertically oscillating upright plate: an experimental investigation. *J. Fluid Mech.* **295**, 263–300.

ZARRUK, G. A 2005 Measurement of free surface deformation in PIV images. *Meas. Sci. Technol.* **16**, 1970–1975.